

## Production, outflow velocity, and radial distribution of H<sub>2</sub>O and OH in the coma of comet C/1995 O1 [Hale-Bopp] from wide field imaging of OH.

Walter M. Harris<sup>1</sup>, Frank Scherb<sup>1</sup>, Edwin Mierkiewicz<sup>1</sup>, Ronald Oliverson<sup>2</sup>, and Jeffrey Morgenthaler<sup>1</sup>.

<sup>1</sup> University of Wisconsin-Madison; 1150 University Ave. Madison, WI 53706; 608-265-3436

<sup>2</sup> Goddard Space Flight Center

### Abstract:

Observations of OH are a useful proxy of the water production rate ( $Q_{\text{H}_2\text{O}}$ ) and outflow velocity ( $V_{\text{out}}$ ) in comets. We use wide field images taken on 03/28/1997 and 04/08/1997 that capture the entire scale length of the OH coma of comet C/1995O1 (Hale-Bopp) to obtain  $Q_{\text{H}_2\text{O}}$  from the model-independent method of aperture summation. We also extract the radial brightness profile of OH 3080 Å out to cometocentric distances of up to  $10^6$  km using an adaptive ring summation algorithm. Radial profiles are obtained as azimuthal averages and in quadrants covering different position angles relative to the comet-Sun line. These profiles are fit using both fixed and variable velocity 2-component spherical expansion models to determine  $V_{\text{OH}}$  with increasing distance from the nucleus. The OH coma of Hale-Bopp was more spatially extended than in previous comets, and this extension is best matched by a variable acceleration of H<sub>2</sub>O and OH that acted across the entire coma, but was strongest within  $1-2 \times 10^4$  km from the nucleus. This acceleration led to  $V_{\text{OH}}$  at  $10^6$  km that was 2-3 times greater than that obtained from a 1P/Halley-type comet at 1 AU, a result that is consistent with gas-kinetic models, extrapolation from previous observations of OH in comets with  $Q_{\text{H}_2\text{O}} > 10^{29} \text{ s}^{-1}$ , and radio measurements of the outer coma Hale-Bopp OH velocity profile. When the coma is broken down by quadrant, we find an azimuthal asymmetry in the radial distribution that is characterized by an increase in the spatial extent of OH in the region between the orbit-trailing and anti-sunward directions. Model fits to this area and comparison with radio OH measurements suggest greater acceleration in this region, with  $V_{\text{OH}}$  up to 1.5 times greater at  $10^6$  km radial distance than elsewhere in the coma.

## 1.0 Introduction:

The study of conditions in comet comae must necessarily begin with an understanding of water. As the dominant volatile component liberated from comet nuclei, the production rate, source geometry, temperature, outflow characteristics, solar wind interaction, and photochemical evolution of water sets the stage for much of the activity in the coma. Water has no visible or UV emission lines and is thus difficult to measure directly. While direct observations of cometary water are now performed over small fields of view in the IR (Dello Russo et al. 2000), historically, the most effective methods for deriving the characteristics of water over the entire coma have been from studies of its daughter products, H, O, and OH. The distribution and/or brightness of each daughter species may be used to derive water production, provided specific knowledge of an appropriate set of physical characteristics (e.g. formation rate, lifetime, outflow velocity, radial distribution, etc.) is available. The ancillary parameters will vary depending on the daughter species studied and are known to differing degrees of accuracy that depend on the solar radiation field, heliocentric velocity, and the total gas production from the comet. The interpretation of water production and evolution from a single measurement or species will therefore vary with the degree of uncertainty in the underlying assumptions (Schleicher, Millis, & Birch 1998). Fortunately the different aspects of water production are complementary and greatly improved convergence is obtained from coordinated observations (Combi et al. 2000).

This paper contains a detailed examination of the production rate, radial distribution, and velocity structure of OH in C/1995 O1 (Hale-Bopp) from wide-field images taken during a 2 week period bracketing its perihelion passage. Hale-Bopp was a unique object in the modern astronomical era, one that provided our best opportunity to date to study the physical properties of water production and evolution, and the effects of collisional processes in the coma at the extreme end of the gas production scale of comets. Because of the high level of Hale-Bopp's activity we could overcome several magnitudes of atmospheric attenuation and extract the radial distribution of OH out to distances  $>10^6$  km from the nucleus. Over such a field of view (FOV), we imaged the entire scale length of OH, and could thus derive  $Q_{\text{H}_2\text{O}}$  using only the  $\text{H}_2\text{O} \rightarrow \text{OH}$  branching ratio, rather than relying on models of coma dynamics. The outer portion of the radial distribution is most sensitive to the outflow properties of OH, and so we fit the radial profiles with two types of spherical expansion models to determine the first order velocity structure of the coma as an azimuthal average and over position angle (PA) sectors relative to the comet-sun line. The model fits show evidence of acceleration over most of the coma that breaks down in regions characterized by a strong velocity gradient within a few  $\times 10^4$  km of the nucleus and a slower process acting over greater distances. These results compare favorably with conclusions

derived from more detailed gas-kinetic models (Combi et al. 1997) and other complementary observations of OH (Colom et al. 1997; Woods, Feldman, & Rottman 2000) and other coma volatiles (Biver et al. 1997). We also report on the presence of an extended OH radial distribution in the trailing sectors of the coma that has also been seen in observations of metastable O ( $^1D$ ) (Morgenthaler et al. in press) and we provide a discussion of some possible mechanisms that could produce it.

## 2.0 Techniques for using OH as a Proxy for $Q_{H_2O}$ and $V_{OH}(r)$ :

OH is a good candidate for deriving  $Q_{H_2O}$  and other dynamical properties of the coma. It has only one significant formation pathway ( $H_2O$ ), whereas the other water byproducts, O and H, may be both daughters *and* grand-daughters of  $H_2O$ , in addition to having multiple parents (in particular O may come in significant quantities from CO and  $CO_2$ ). O and H emissions have other complicating characteristics, such as collisional quenching of O ( $^1D$ ) (Schultz et al. 1993) and Hydrogen's complex velocity structure (Smyth et al. 1993), large scale length, and interactions with solar wind and radiation field. By contrast,  $\sim 90\%$  of OH is formed directly from  $H_2O$  into the  $X^2 \text{ II}$  ground state (Budzien, Festou, & Feldman 1994; Van Dishoeck & Dalgarno 1984), which results in the brightest, highest contrast resonance fluorescence emission that is accessible from ground-based telescopes. The OH scale length against photodestruction is much shorter than for O or H (Huebner, Keady, & Lyon 1992), and it may thus be imaged in its entirety.

The OH life cycle in the comet follows three primary steps beginning with the photo-destruction of  $H_2O$ , followed by a radial expansion away from the nucleus, and ending with its dissociation or ionization. This chemical pathway ( $H_2O \rightarrow OH \rightarrow O + H, OH^+$ ) has been studied extensively both theoretically and observationally (Budzien, et al. 1994; Schleicher & A'Hearn 1988; Van Dishoeck & Dalgarno 1984), and, while recent observations of O( $^1D$ ) suggest that the dissociation branching ratios of OH to its daughters may need to be reviewed (Morgenthaler, et al. in press), the overall lifetime, state structure, and fluorescence efficiency of OH appear to be relatively well understood as functions of solar flux and heliocentric velocity. Because these various parameters all contain information about the evolution of water in the coma, to the extent that they are known, it is possible to invert the OH distribution to a map of water production either by fitting outflow models to the observed radial distribution or by adding all of the photons from the OH coma.

### 2.1 $Q_{H_2O}$ from Aperture Summation:

If the angular extent of the coma is smaller than a telescope FOV, and the signal level of OH is great enough to overcome atmospheric extinction, one may sum all the photons in the

FOV and determine  $Q_{OH}$  (and thus  $Q_{H_2O}$ ) with knowledge of only the g-factor, the lifetime against OH photo-dissociation, and the branching ratio from  $H_2O$ . With this technique  $Q_{H_2O}$  is derived from

$$1) Q_{OH} = N_{OH} \Omega \Delta^2 / \tau_{OH},$$

where  $\Omega$  is the solid angle of the FOV,  $\Delta$  is the geocentric distance,  $\tau_{OH}$  is the photochemical lifetime of OH, and  $N_{OH}$  is the average column density over the field of view. The column density comes from the total signal in the aperture

$$2) N_{OH} = 10^6 I_{OH} / g,$$

where  $I_{OH}$  is the field-averaged brightness in rayleighs and the fluorescence efficiency,  $g$ , is adjusted for heliocentric Doppler shifts across the Solar Fraunhofer spectrum at 3080 Å (Schleicher & A'Hearn 1988). The conversion to  $Q_{H_2O}$  (Table 1) is made by dividing  $Q_{OH}$  by  $BR_{OH}$ , the branching ratio of water dissociation to OH (Table 2).

The principle advantage of aperture summation for the determination of  $Q_{H_2O}$  is that it does not require any specific knowledge of the structure of the coma, and is therefore not dependent on models of the radial distribution. Its primary disadvantage is that it provides only  $Q_{H_2O}$ , without any understanding of the characteristics of the coma.

## 2.2 Outflow Velocity:

Maps of the OH velocity and spatial distribution can be directly tied to the gas production and outflow characteristics of the coma as function of radial distance. The radial extent and velocity distribution depends on a combination of factors including  $Q_{H_2O}$ , solar UV radiation intensity, heliocentric velocity/distance, and collisional effects. When the field of view of a measurement is smaller than the radial extent of the OH coma, knowledge of the velocity is also required to invert the OH brightness distribution to  $Q_{H_2O}$  (Cochran & Schleicher 1993), because velocity and production are directly proportional in a spherically expanding flow.

The OH velocity distribution is the result of a convolution between the outflow characteristics of the parent  $H_2O$  molecules, the effect of any subsequent collisions of OH with coma constituents, and the excess energy of formation, which contributes a random velocity vector with a magnitude of 1.05 km/sec (Huebner, et al. 1992). The spatial extent of the OH coma is defined by the velocity distribution, the dimensions of the source region, the heliocentric distance of the comet, and the solar UV intensity. In most comets the velocity distribution of OH in the coma not known directly, and must be determined by fitting models to the radial shape of the coma or by assuming a uniform outflow velocity with a dependence on heliocentric distance ( $R_h$ ) given by

$$3) V_{\text{OH}} = 0.85 R_h^{-2}$$

(Budzien, et al. 1994). Aside from the few *in situ* measurements (Lammerzahl et al. 1987) that serve as a basis for the above equation, wide-field, aperture-averaged measurements of the line profile of radio OH emissions (Bockelée-Morvan, Crovisier, & Gerard 1990; Colom, et al. 1997) are the only direct means we have for observing  $V_{\text{OH}}$ . Radio measurements generally validate the standard relation in an average sense for comets with  $Q_{\text{H}_2\text{O}} < 10^{29} \text{ s}^{-1}$ , but obtain higher velocities for more active comets ( Bockelée-Morvan, et al. 1990). A major limitation of using radio OH line profiles for  $V_{\text{OH}}$  is that the emissions are strongly quenched (Schloerb 1988). The effect of this is to bias the extracted velocity to the outer coma, masking structure in the velocity distribution with cometocentric distance. This is not a concern for comets with a mostly ballistic coma, but it is a serious problem in active ( $Q_{\text{H}_2\text{O}} > 10^{30} \text{ s}^{-1}$ ) comets like Hale-Bopp, where photolytic heating (see section 2.3 below) acts to raise the temperature of the gas and increase the bulk outflow velocity with increasing distance from the nucleus. In the absence of any physical data on the velocity distribution, the OH radial distribution must be blindly matched with models that track the evolution of water in the coma (Combi & Smyth 1988a; Combi & Smyth 1988b; Hodges 1990).

Fitting velocities to the OH radial distribution while assuming the lifetime-related parameters are known is a primary method for determining  $V_{\text{OH}}$ . This can be done in a variety of ways, ranging from variable width aperture photometry (Colom, et al. 1997; Schleicher, et al. 1998) to sophisticated hydrodynamic (Crifo 1995) or Monte-Carlo simulations (e.g. Hodges 1990; Combi and Smyth 1988a,b). The extent to which these techniques produce unique results is determined by the accuracy with which  $Q_{\text{H}_2\text{O}}$  is known and the radial distance out to which the OH brightness has been measured. It is the outermost regions of the coma that are most sensitive to  $V_{\text{OH}}$  (Cochran & Schleicher 1993). When distances less than the OH scale length are sampled, spherical expansion models will produce a ‘family’ of velocity fits that are all of equal quality, but indicate different values of  $Q_{\text{H}_2\text{O}}$ . The range of acceptable velocities and hence the convergence of model fits of  $V_{\text{OH}}$  improves with the increasing radial extent of the sampled profile. A combination of radial maps of the OH distribution and wide field summations of the OH velocity profile (Colom, et al. 1997) further constrain the outer coma velocity and indicate the extent and magnitude of acceleration in the inner coma.

### 2.3 The Collision Zone:

Hale-Bopp is an extreme example of a comet where collisional acceleration acts across a spatially resolved region of the coma, affecting the interpretation of both OH radial profiles and outer coma velocity measurements. Where collisions dominate, the characteristics of the flow

will be modified toward a thermalized average of *all* species (parent, daughter, ion, electron, dust, etc.) that are present. Energy input will come from daughter velocity excesses resulting from photo-dissociation (dominated by fast H atoms) and ionization as the gasses traverse the collision zone, a process that is similar to photolytic heating in planetary upper atmospheres. It is possible to estimate the size of the collision zone by adopting the simplifying assumption of a spherically symmetric expanding coma with negligible dust mass loading. From this a simple formula (Whipple & Huebner 1976) for the collision zone radius ( $r_c$ ) is

$$4) \quad r_c = \sigma Q_{\text{TOT}} / 4 \pi V,$$

where  $\sigma$  is the mean molecular cross section for ballistic collisions,  $Q_{\text{TOT}}$  is the total gas production rate of the comet (dominated by  $\text{H}_2\text{O}$ ), and  $V$  is the mean outflow velocity of the background gas. The transition from a thermalized distribution to ballistic flow is a gradual, extending over distances greater than  $r_c$ . Models of the 1P/Halley velocity structure (Hodges 1990) showed that, while the flow was largely ballistic by  $6 \times 10^4$  km from the nucleus, there was residual collisional heating out to  $> 2 \times 10^5$  km.

The relevance of equation 4 depends on the amount of gas production. For weak to moderately active comets at 1 AU with  $Q_{\text{H}_2\text{O}} \leq 10^{29} \text{ s}^{-1}$ ,  $V_{\text{H}_2\text{O}} = 0.87 \text{ km-s}^{-1}$  (Budzien et al., 1994), and  $\sigma \sim 3 \times 10^{-15} \text{ cm}^2$ , the size of the collision zone is of order 1000 km or less at 1 AU. This is smaller than the scale lengths of most coma species and limits the effect of photolytic heating in the coma. Such a collision zone will also be unresolved for most observations, which means that any acceleration that occurs within it will be detectable only as an increase in the uniform bulk flow that becomes larger along with the gas production rate.

For very active comets with  $Q_{\text{H}_2\text{O}} \geq 10^{30} \text{ s}^{-1}$ , the collision sphere will be resolvable and begin to approach the dimensions of the scale lengths of  $\text{H}_2\text{O}$  and OH, which means that a significant fraction of all water photochemistry will occur in a collisionally thick medium. Both models (Combi, et al. 1997; Combi & Smyth 1988b; Hodges 1990) and observations (Bockelée-Morvan et al., 1990) show that this results in a significantly hotter coma that flows more rapidly away from the nucleus. Several estimates of  $Q_{\text{H}_2\text{O}}$  obtained using different methods (Colom, et al. 1997; Combi, et al. 2000; Woods, et al. 2000) converge to values near  $10^{31} \text{ s}^{-1}$  for Hale-Bopp at perihelion, which corresponds to  $r_c > 3 \times 10^5$  km, assuming  $V \sim 1 \text{ km s}^{-1}$ . This distance exceeds the scale length of water and several other coma species (both parent and daughter) at 1 AU, and the resulting increase in energy deposition modifies the magnitude and the spatial evolution of the outflow velocity, the excess velocity distributions of the daughter species, and the temperature of the gas.

### 3.0 Observations of OH:

The OH observations of Hale-Bopp were taken using the Burrell Schmidt Telescope, which was operated in 1997 by the Kitt Peak National Observatory (KPNO) and Case Western Reserve University. The Burrell is a 0.9 m Schmidt Cassegrain with a UBK7 corrector that provides system sensitivity down to 3050 Å. For Hale-Bopp the telescope was fitted with a KPNO SITE 2048 x 2048 CCD camera covering a 78.9' FOV. Observations of OH were obtained as part of two runs (March 24-29; April 8) that bracketed perihelion. The Burrell FOV exceeded  $10^7$  km for Hale-Bopp over this period, a radial extent roughly two orders of magnitude greater than the OH scale length in a Halley-class or weaker comet. The images were taken using the OH filter of the Hale-Bopp comet library (Farnham, Schleicher, & A'Hearn 2000) in single binning mode. The observations are summarized in Table 1.

### 3.1 Calibration and Correction for Atmospheric Attenuation:

Atmospheric attenuation was the most serious calibration issue for OH 3080 Å imaging (Farnham, et al. 2000). The already strong function of OH opacity to airmass was exacerbated by the low elevation of Hale-Bopp on most nights during this period. The comet began each night at its maximum elevation, which, over our time frame, ranged between 30° and 21° or 2-3.5 airmasses (Table 1), and set within 4 hours. OH images were taken on each night, but the most useful data were obtained on March 28 and April 8, 1997, when setup, acquisition and focus were procedurally perfect, and where OH was the immediate priority for observation. The data from April 8 is of higher quality due mainly to the smaller airmass. There were no standard stars bright enough at 3080 Å to be detected in the FOV of the comet images, so we obtained a series of observations of  $\alpha$  Aur cover the same range of elevation angles to use as a flux standard. The stellar images were calibrated with IUE spectra at 3100 Å and used to derive a relationship between airmass and attenuation. We interpolated between the images to the corrections at the comet elevations, and assign a conservative ~15% accuracy in comet OH intensities.

### 3.2. $Q_{H_2O}$ From Aperture Summation:

In the full-aperture summation extraction, the flat-fielded, bias and dark subtracted images were converted to a series of concentric variable diameter apertures centered on the comet nucleus. The total flux was co-added until increasing the area of the aperture failed to improve the signal to noise of  $I_{OH}$  and a comparison with the ring summing results indicated that the scale length had been reached. The total ADU were converted to rayleighs, and from then to  $N_{OH}$  and  $Q_{H_2O}$  using equations 1 and 2 above.

### 3.3. Ring Summation and the OH Radial Brightness Distribution:

Extraction of the OH spatial distribution was performed using a dynamic ring summing algorithm that operated by extracting all pixels over a range of radial distance and position angle, filtering for salt and pepper noise, and then coadding to obtain an average. Radial profiles of OH distribution were constructed by coadding annuli centered on the nucleus, with the annulus width in pixels set to the smallest value that maintained  $s/n > 4$ , up to a maximum of 75 pixels or  $1.75 \times 10^5$  km. Full azimuthal coma averages and sub-arcs  $90^\circ$  and  $30^\circ$  in extent were extracted using this method. The ADU/ring averages were again converted to rayleighs based on the  $\alpha$  Aur calibration.

## 4.0 Results:

### 4.1 $Q_{H_2O}$ from Aperture Summation of $I_{OH}$ :

Following the conversion of ADU to rayleighs, we obtain  $Q_{OH} = 7.9 (\pm 1.2) \times 10^{30} \text{ s}^{-1}$  on 03/28 and  $9.17 (\pm 1.4) \times 10^{30} \text{ s}^{-1}$  on 04/08 using the aperture summation method. With  $BR_{OH} = 0.86$  (Table 2, Huebner, et al. 1992), this corresponds to  $Q_{H_2O} = 9.31 (\pm 1.4) \times 10^{30} \text{ s}^{-1}$  and  $10.8 (\pm 1.6) \times 10^{30} \text{ s}^{-1}$  on the two dates respectively (Table 1). These values compare favorably with other measurements of  $Q_{OH}$  made over the same period using a similar technique (Woods, et al. 2000).

### 4.2 Ring Summation Azimuthal Average:

The coma-averaged OH surface brightness distributions show evidence of substantial acceleration both from the spatial extent of the emission and the profile gradient inside  $10^4$  km. Figure 1 compares the measured OH radial profile on 8 April with a simple 2-component Haser simulation based on the 0.89 km/s spherical outflow derived from 1P/Halley and other comets at a heliocentric distance of 1 AU (Budzien, et al. 1994; Lammerzahl, et al. 1987). It is possible to scale the model to fit the observed profile out to a distance of  $\sim 1-2 \times 10^5$  km and derive a water production rate of  $Q_{H_2O} \sim 6 \times 10^{30} \text{ s}^{-1}$ . However, the model fails on larger spatial scales as the scaled fit falls off while the OH distribution continues outward. Indeed, there is no scale factor that will allow a Halley-like flow to describe the outer regions of Hale-Bopp's OH coma, nor one that will match the inner coma radial distribution and provide  $Q_{OH}$  equivalent to that obtained from aperture summation in the same image. A higher outflow velocity is required to fit the extended part of the profile (see below), and, since  $Q_{H_2O} \propto v/e^{(-\tau/v)}$ , a higher production rate is indicated as well.

### 4.3 Ring Summation by Quadrant:

To look for azimuthal structure and asymmetries in gas production and radial extent of the emission we divided the coma into four 90° sectors of position angle (PA). We chose quadrant dimensions approximately centered on the comet-Sun line to allow comparison of day vs. night side gas production. The PA of the anti-Sun vectors on March 28 and April 8 are given in table 1. Due to the favorable viewing geometry near perihelion, the PA of the orbital velocity vector was well separated from the anti-Sun vector, which meant that the dust tail and anti-tail directions could also be isolated into separate quadrants, giving us four distinct coma environments for comparison.

The individual quadrants show significant differences in the spatial extent of the emission and shape of the profiles. This is consistent with a sun-comet angle/orbital phase dependence in the acceleration (Figure 2a,b). Moving radially outward in the sunward and anti-tail (orbit leading) quadrants, the OH surface brightnesses are greater than in the anti-sun and tailward (orbit trailing) quadrants out to  $\sim 10^5$  km from the nucleus. Beyond this point the leading quadrant profiles begin to steepen and become progressively weaker relative to the trailing direction, with the profile in the sunward direction always the least spatially extended. The magnitude of the difference in spatial extension varied between the observations, however the leading/trailing profile asymmetry was a consistent feature on both dates studied, and does not appear related to the effects of short term  $Q_{H_2O}$  variability. Assuming a uniform gas source distribution, the differences between the quadrant radial distributions are indicative of less acceleration occurring in the leading quadrants.

To get at the detailed structure of the spatial extension in the trailing direction we divided these quadrants into 30° sub-sector profiles. The sub-sectors show that the majority of the spatial extension can be isolated to an  $\sim 60^\circ$  PA range centered slightly anti-sunward of the dust tail and extending into the region between the dust and ion tails (Figure 2c,d). The enhancements themselves were not tightly confined, but extended into the adjacent sub-sectors with the amount of extension diminishing away from the peak back to the levels seen in the leading quadrants. The most extended sub-sectors appear to contribute most of the extended emission in the quadrants where they are present, and, more significantly, appear to dominate the spatial extent of the azimuthally averaged radial profile. While the position angle of the peak in extension does vary slightly between these dates, the basic morphology of the spatial asymmetry extension and its effect on adjacent sub-sectors did not. The location and extension of the enhanced regions are also consistent with a similar feature reported in wide field O ( $^1D$ ) images taken three weeks prior to our observations (Morgenthaler, et al. in press).

## 5.0 Coma Simulation Techniques:

The azimuthally averaged and sector OH radial distributions were fit using different forms of a 2-component Haser model (Haser 1957; Krishna Swamy 1997). We employ the Haser approach over the typically more accurate vectorial model (Festou 1981a), because the latter assumes a daughter product velocity distribution resulting from photodissociation in the purely ballistic case, a condition that did not hold over most of the scale length of the H<sub>2</sub>O parent in Hale-Bopp. Spherical expansion models are not physically accurate. They do not address extended source (icy grain) regions, azimuthal asymmetries, or temporal variations in gas production, but they nevertheless have proven useful for estimating outflow velocities and gas production rates when applied outside of the collisionally thick coma. They are also computationally simple, which lets us quickly sample a broad range of input parameters to fit data. Our limited aims in using such models here are to determine that acceleration is occurring over a significant extent of the coma of Hale-Bopp, to compare our results with more sophisticated models and other observations, and to define the range of initial and final outflow velocities and production rates that describe the observed OH distribution.

We use two types of outflow approximations. In the first case, both  $V_{\text{H}_2\text{O}}$  and  $V_{\text{OH}}$  are held fixed throughout the coma, but may vary independently of one another. In the second, we simulate collisional mixing and acceleration by forcing  $V_{\text{H}_2\text{O}} = V_{\text{OH}}$  while allowing the combined flow to increase with cometocentric distance. The other physical parameters that describe H<sub>2</sub>O/OH photochemistry and fluorescence, including g-factors and lifetimes (Table 2), are set to the appropriate solar cycle, heliocentric distance, and Swings effect values found in the literature (Budzien, et al. 1994; Schleicher & A'Hearn 1988). Each velocity simulation consists of the different runs of the model over three different spatial scales in the coma,  $r < 10^5$  km,  $10^5 \leq r < 10^6$ , and the full profile out to  $10^6$  km. The model profiles are then fit to the data to obtain a point by point least squares difference that is then co-added for each of three sub-sections. An overall fit quality index for each case is derived from the product of the three summed differences. By merging the fits on different spatial scales we were able to screen out velocity combinations that fit large regions of the profile very well, but were obviously wrong at the extremes. This was particularly important for the profile at large radial distances.

### 5.1 The Fixed Model:

We use the classical form of a fixed velocity 2-component Haser model (Krishna Swamy 1997) where the parent and daughter velocities are fixed as a function of radial distance, but may be different from one another with restriction that  $V_{\text{OH}} \geq V_{\text{H}_2\text{O}}$ . For weaker comets,  $V_{\text{OH}}$  is roughly equal to  $V_{\text{H}_2\text{O}}$ , differing only by the convolution of  $V_{\text{OH}}$  with the 1.05 km-s<sup>-1</sup> excess velocity of H<sub>2</sub>O dissociation (e.g. Festou, 1981a ). The usefulness of the fixed model is that

when  $V_{\text{OH}}$  and  $V_{\text{H}_2\text{O}}$  differ by more than the excess velocity, it indicates the presence of acceleration in the coma, with the magnitude of the velocity ratio indicating the steepness of the velocity gradient. On the negative side, when there is acceleration over a spatially resolvable area of the coma, the fixed velocity flow model is an unphysical approximation of conditions, because it treats the velocity gradient only as a difference between  $V_{\text{OH}}$  and  $V_{\text{H}_2\text{O}}$ . Such a condition exaggerates the difference in initial and final velocities, since collisions will drive both  $\text{H}_2\text{O}$  and  $\text{OH}$  to a single radial velocity throughout the inner coma, while the model must assume that  $\text{H}_2\text{O}$  is always slow and  $\text{OH}$  is always fast. This requirement leads to contradictory model requirements, and errors in the fit.  $V_{\text{H}_2\text{O}}$  must be small to offset the high  $V_{\text{OH}}$  in the inner coma, but this prevents  $\text{H}_2\text{O}$  from reaching the outer coma where it can produce  $\text{OH}$ . With a minimal source of outer coma  $\text{H}_2\text{O}$ , the model responds by increasing  $Q_{\text{H}_2\text{O}}$  and  $V_{\text{OH}}$  to make up the difference.

This model was used for a range of velocities from 0.25 to 5.0  $\text{km}\cdot\text{s}^{-1}$  to obtain sets of local minima of fit index vs.  $V_{\text{OH}}$  for a given  $V_{\text{H}_2\text{O}}$  in both the coma averaged case and the four quadrants. The full set of minima values were further winnowed by stepping through  $V_{\text{H}_2\text{O}}$  to find lowest fit indices over all of velocity space. A comparison with  $Q_{\text{OH}}$  implied by the model vs. aperture summation was used as an external validity check, but not as a fitting criterion. The best runs all match the observed profiles closely (Figure 3a), including the spatially extended sectors (Table 3). The utility of measuring the distribution out to a large radial distance is reflected in the convergence of the results. The fit families of the velocity and production rates vary only within 10%, which is better than our photometric accuracy. However, despite the quality of the fits, our results underscore the limitations of using a fixed model for an accelerating coma. The most obvious manifestation of this is the failure of the model to provide  $Q_{\text{H}_2\text{O}}$  consistent with aperture summation or an outer coma  $V_{\text{OH}}$  similar to those directly measured by Colom et al., (1997). The calibrated fits to the spherically averaged brightness profiles yield  $Q_{\text{H}_2\text{O}} \sim 30\text{-}50\%$  higher than from the aperture method or other estimates (Combi, et al. 2000; Woods, et al. 2000), and  $V_{\text{OH}} \sim 50\text{-}100\%$  higher than in direct measurements by Colom et al. (1997). In the case of the more extended trailing sectors, these differences become even more exaggerated.

We take the fact that the best matches to the data were invariably those with a substantial velocity difference between  $V_{\text{OH}}$  and  $V_{\text{H}_2\text{O}}$  as evidence for significant acceleration in the coma. Figure 4 shows the relationship between  $V_{\text{OH}}$  and  $V_{\text{H}_2\text{O}}$ . We note that even when a uniform ( $V_{\text{OH}} = V_{\text{H}_2\text{O}}$ ) outflow can be fit to the full radial profile, it does not match the shape very well. Indeed, the best uniform outflow cases produce higher fit indices than the minima for all other velocity ratios and are more than 100x larger than the best mixed velocity ( $V_{\text{OH}} \neq V_{\text{H}_2\text{O}}$ ) case.

The clear inference from this is that acceleration was occurring over a large region of the coma of Hale-Bopp rather than in a small, unresolved area near the nucleus. Furthermore, if we assume a uniform flow and thus take the weighted average velocity ( $V_{AV}$ ) of the combined parent-daughter distribution in the model fits as

$$4) \quad V_{AV} = (N_{OH} * V_{OH} + N_{H_2O} * V_{H_2O}) / (N_{OH} + N_{H_2O}),$$

where  $N_{OH}$  and  $N_{H_2O}$  are the column densities of these species, we obtain radial velocity profiles showing a strong inner coma velocity gradient that diminishes beyond the water scale length and is similar to theoretical predictions.

## 5.2 Simulations of Variable Velocity Expansion:

An improvement in the physical accuracy of the model profiles may be achieved by adopting a single parent-daughter velocity that changes with cometocentric distance; i.e. an accelerating flow. Accelerating spherical expansion models (Hu 1990) are typically avoided, because the acceleration regions of most comets are confined to the unresolved extreme inner coma, and because the Haser approach offers no insight into the nature of the acceleration or how to address it. To avoid taking an entirely ad hoc approach to this problem, we draw from the basic elements of the more detailed 1-D dusty-gas simulations of Combi et al. (1997) as a starting point for developing a simple variable velocity spherical expansion model. Their approach has the coma effectively breaking down into two acceleration regions. Close to the nucleus, fast H atoms formed by  $H_2O$  and OH dissociation are re-thermalized into the bulk flow. This leads to a substantial acceleration out to the cometocentric distance where H collisionally decouples from the background gas, a location that is defined by the total gas production rate and heliocentric distance. Past this point the primary sources of acceleration are a diminishing collisional component and a passive filtering of the thermal distribution where the slower OH molecules are photodissociated closer to the nucleus than the faster ones, thus leaving a progressively higher velocity remnant with increasing distance. The collisional and passive acceleration zones are approximated in our simulations with different linear velocity gradients on either side of a contact radius.  $V_{OH} = V_{H_2O}$  at all locations in this model, with the initial velocity, velocity gradients, and the location of the H contact radius serving as input variables. We don't include the excess velocity of OH formation from  $H_2O$  in our calculations because it is a non-radial velocity component, we have no information on how the excess is affected by collisions, and because the actual outflow velocity of Hale-Bopp was considerably higher than 1.05 km/sec.

The accelerating model produces fit indices 10 times smaller than those obtained from the fixed model and better agreement with both the aperture summation  $Q_{OH}$  derivation and direct measurements of  $V_{OH}$ . A point-by-point least squares fit analysis shows the improvement

in fit is due primarily the quality of the match in the outermost part of the radial profile, which is where the shape is most sensitive to the presence of acceleration in the outer coma. Our best results are for a substantial change in velocity across a relatively small region within  $\sim 1\text{-}2 \times 10^4$  km of the nucleus, followed by a much shallower gradient at larger distances (Table 3; Figure 3b). These fits consistently indicate an initial velocity ( $\sim 1.0 \text{ km-s}^{-1}$ ) that is quite close to the measured range of less active comets at the same heliocentric distance (Budzien, et al. 1994) and inner coma velocity dispersion measurements (Biver, et al. 1997). Acceleration in the model continues throughout the coma, such that the outflow velocity eventually reaches a larger value ( $2.3\text{-}2.6 \text{ km-s}^{-1}$ ) similar to other outer coma measurements (Colom, et al. 1997).

Inverting the model profiles to production rates results in a range of  $Q_{\text{H}_2\text{O}} = 0.8\text{-}1.0 \times 10^{31} \text{ s}^{-1}$  for both dates, which are much closer to the results of aperture summation. The derived  $Q_{\text{H}_2\text{O}}$  for the quadrants is also more uniform with PA in this model output than in the fixed case, which we expect if the  $\text{H}_2\text{O}$  velocity is allowed to change and acceleration can occur beyond the edge of the  $\text{H}_2\text{O}$  scale length.

The model results by quadrant again show that the leading hemisphere is less accelerated than the trailing one, with the most spatially extended sectors being fit by a larger outflow velocity at  $10^6$  km than those in the leading hemisphere. The largest velocity gradients in the coma average and trailing hemisphere are found inside the collision sphere, although most of the acceleration occurs in the outer coma, where the velocity gradient is significantly smaller, but occurs over a substantially greater distance. On 28 March, the leading sectors of the coma were fit best by an acceleration profile that had no gradient inside the collision zone. Whether this is an artifact of the model or indicative of a physical mechanism such as dust mass loading (Colom, et al. 1997) is not clear from our simple treatment.

## **6.0 Comparisons of the Model Velocity Distribution with Other Data and Models:**

### **6.1 Radio Outflow Velocity Measurements:**

We compared the results of our models with the aperture summed radio measurements of Colom et al., (1997) and Biver et al. (1997) by computing a number density weighted, line-of-sight integrated velocity at each radial distance from the nucleus, weighting them by the area of their ring, and then co-adding all of the rings to obtain an average outflow velocity. The main caveat to this approach is that our simple model produces line of sight velocities assuming pure radial expansion without vectorial or thermal dispersion in the velocity distribution. However, the trapezoid method ( Bockelée-Morvan, et al. 1990) used in the reduction of the radial data isolates only the radial velocity component, which is the equivalent of our model velocities. The comparison with the divergent fields of view of the radio measurements serves a check on the

model and the assumed OH quenching characteristics.

### 6.2.1 Inner Coma Velocities:

Biver et al. (1997) provide velocities over different regions of the inner coma, but they do not specifically measure OH. Indeed they can't, since virtually all of it would be quenched at such small distances from the nucleus (Schloerb 1988; Schloerb et al. 1997). Instead, they use several different species including HCN, CO, H<sub>2</sub>S, CH<sub>3</sub>OH, CS, and H<sub>2</sub>CO to derive the expansion velocity over the  $1.5 \times 10^4$  km half-power width of their beam. Given the extent of the collision sphere, and clear evidence for acceleration across the inner coma, it is reasonable to assume that the outflow at any given point over this region is the same for all gas species. On the other hand, each constituent of the coma will have different radial characteristics depending on its scale length, whether it is a parent or a daughter species, or whether it has an extended source distribution. A substantial variation in aperture averaged  $V_{\text{outflow}}$  will be obtained from the different species, with most of the difference due *only* to the spatial distribution of the sources. The extent to which Biver et al. (1997) was able to account for this in their measurements is unclear, but it must have been a significant effect given the spread of scale lengths for the species they measured. For our purposes, we ran a variable velocity simulation for the best fit case of acceleration parameters for the OH radial distribution, using a species with a scale length equal to that of HCN (Huebner, et al. 1992) and assuming a nucleus-centered source. Using figure 2 of Biver et al., we find an HCN outflow velocity of  $1.4 \pm 0.1$  km/s for the period surrounding perihelion. Our model value of  $V_{\text{H}_2\text{O}} = 1.2 \pm 0.15$  km/s is within the relative uncertainties of the different results.

### 6.2.2 Intermediate Distances:

Colom et al. (1997) directly measured the velocity of OH over a much larger area with an asymmetric ( $3.5' \times 19'$ ;  $200000 \times 110000$  km) beam and obtained an average outflow velocity of 2.2 km/s. We are able to compare our model with this result, with the primary caveat that we must also address the effect of quenching in the radio measurements. Schloerb et al. (1997) computed the OH quenching radius ( $R_Q$ ) for Hale-Bopp to be  $5 \times 10^5$ . Since only OH molecules at distances  $\geq R_Q$  are detectable in radio observations, Colom et al. (1997) therefore measured a velocity average that was strongly biased to the outer coma. This will result in a higher coma averaged velocity in the radio relative to our unquenched model fit, with the size of the difference indicative of the magnitude of the acceleration and the spatial extent over which it occurs in the undetected areas of the coma. For example, a collision zone confined to the immediate vicinity of the nucleus will result in only a minimal difference between a quenched velocity and an unquenched one. Thus, the difference in our modeled area averaged outflow of

1.7 km/s when compared to their radio measurement of 2.2 km/s implies a broad acceleration region in Hale-Bopp. We can carry the comparison further by incorporating quenching effects in our model such that we restrict the contributing OH emission to a shell surrounding the nucleus with an inner radius equal to  $R_Q$ . Averaging only the velocities in this extended region of the coma results in a simulated average velocity of  $2.3 \text{ km-s}^{-1}$ , which is closer still to the measured value of Colom et. al. (1997).

### 6.3 Comparison with Observational and Theoretical Predictions:

Very little data exists on the characteristics of comets with  $Q_{\text{H}_2\text{O}} \sim 10^{31} \text{ s}^{-1}$ , and most of the predictions are merely an extension of the behavior of weaker comets to this scale. In this sense Hale-Bopp is in a class of its own with respect to coma dynamics and provides the best opportunity to date to test the accuracy of these predictions. When  $Q_{\text{H}_2\text{O}} > 10^{31} \text{ s}^{-1}$ , the collision sphere radius exceeds the scale length of water at 1 AU, opacity effects become significant, and other processes, such as parent/daughter/granddaughter collisions, chemistry (e.g. Komitov, 1989) and ion-neutral interactions, may begin to emerge. Bockelée-Morvan et al. (1990) have compiled the most extensive listing of  $Q_{\text{H}_2\text{O}}$  vs.  $V_{\text{H}_2\text{O}}$  in active ( $Q_{\text{H}_2\text{O}} > 10^{29} \text{ s}^{-1}$ ) comets, and their data shows clear evidence of an upturn in the outflow velocity for active comets. Hale-Bopp is a clear validation that this trend continues with increasing activity, though perhaps not to the extent implied by those weaker comets. Cochran and Schleicher (1993) took the Bockelée-Morvan results a step further by fitting them to a power law modification of the standard Q-V relationship

$$5) \quad V_{\text{OH}} = 0.85 r_h^{-2} \times (Q/10^{30})^{0.5},$$

which, as no more than a fit to points on a graph, is a somewhat ad hoc result. From their equation we can obtain a value of  $V_{\text{H}_2\text{O}} \sim 3.25 \text{ km-s}^{-1}$  for a comet with  $Q_{\text{H}_2\text{O}} = 10^{31} \text{ s}^{-1}$  and  $R_h = 0.91 \text{ AU}$ . This is substantially higher than we obtain from the variable velocity model and was observed aperture average velocity (Colom, et al. 1997).

Physical models of collisionally dense comas that include extensive regions of dust/gas interactions and substantial opacity corrections (Combi, et al. 1997; Crifo 1995) may also be extended to the necessary activity scale. We compare our data and simulation results with those of Combi et al. (1997), who used a 1-D spherical hybrid kinetic/dusty gas-hydrodynamic calculation to describe the thermal and velocity characteristics of the outflow with cometocentric distance from the nucleus for Hale-Bopp at different heliocentric distances. The results of our simulations generally agree with the dusty gas predictions, although we expect as much in the case of the variable velocity case, since it was based on the parameters of the Combi et al. (1997) model. However it is also true of the fixed model, where the best fits were for cases with large

differences between the initial and final velocities of the bulk flow, with the average velocity increasing rapidly near the nucleus and more slowly in the outer coma. The notable exceptions to this are the sectors with spatially extended OH emission, which are fit on every spatial scale by significantly *higher* acceleration than the Combi et al. (1997) model indicates at 1 AU.

## **7.0 Potential Sources of the Extended Emissions:**

The OH enhancement in the sector between the anti-Sun and orbit-trailing directions could have one source or several mechanisms acting together to produce it. Some of these are unlikely or can be easily shown to be inadequate. For example, the magnitude of radiation pressure on OH is only enough to accelerate the gas by  $\sim 0.01$  km/s over our field of view. We looked closely at four mechanisms that could produce an apparent enhancement including dust contamination from the tail, distributed gas production from icy grains, dust mass loading in the leading hemisphere, and an ion-neutral interaction.

### **7.1 Dust Contamination:**

While OH emission dominates over continuum in the regions near the nucleus, dust contamination may be significant in the outer parts of the coma where the OH brightness is lower. If improperly accounted for, the dust scattering of solar continuum could produce a false region of enhancement. This effect is most important where the dust is concentrated along the tail and extending back toward the antisunward vector, which is also where the extended OH emission regions are observed. To check this, we made a direct comparison of the radial shape and brightness of the dust over the same angular regions from a visible continuum image obtained on the same night as the April 08 OH data. The image was taken using the Blue Continuum ( $4446 \pm 31 \text{ \AA}$ ) filter of the Hale-Bopp filter library, covering the same field of view. After correcting for instrument sensitivity, atmospheric attenuation, and the brightness of the solar flux at  $3100 \text{ \AA}$  vs  $4450 \text{ \AA}$ , a radial dust profile was extracted over the sub-sector corresponding to the greatest radial enhancement of OH. In direct comparison (figure 6), the dust and OH radial distributions differ on two levels that allow us to eliminate dust as the source of the trailing extension. The shape of the dust profile is significantly shallower with radial distance than OH, while its brightness is only  $\sim 2\text{-}10\%$  that of OH, out to distances  $>10^6$  km.

### **7.2 Grain Evaporation:**

While we can demonstrate that scattered solar continuum from dust does not contribute significantly to the OH radial distribution, the dust lane does cover the area of the enhancement and could thus still affect the OH radial distribution through outgassing from grains in the tail. We cannot possibly to completely exclude this process as a contributor; however it would have

several effects on coma structure that make it an unlikely source of the increased spatial extent of OH. The distribution of evaporative grains would need to be approximately uniform throughout the tail sectors to produce the smooth radial shape seen in the OH data. The source of evaporating grains would have to have been continuous over a period of more than a month to account for the persistence of the feature in OH and O ( $^1D$ ) images (Morgenthaler, et al. in press). Finally, any OH produced beyond  $2 \times 10^5$  km would be in the ballistic coma, and thus not accelerated beyond the convolution of grain motion and the 1.05 km/s excess formation velocity. Because the distribution of OH is dominated by the extended sectors beyond  $5 \times 10^5$  km, such a velocity admixture would be reflected in the aperture summation measurements of Colom et al. (1997) as an average velocity reduction that is not observed.

### **7.3 Dust Mass Loading:**

Several studies of the Hale-Bopp coma have concluded that dust grain production was largely confined to the sunlit hemisphere of the nucleus (Rauer et al. 1997; Weaver et al. 1997), while gas production was more uniformly distributed (Samarasinha, Mueller, & Belton 1997). In the inner coma, where photolytic heating is most effective in accelerating the neutrals, the local dust grain population absorbs collisional energy, thus impeding the acceleration and gas heating. The spatial extent and efficiency of the dust loading process in Hale-Bopp was examined by Combi et al. (1997), who looked at the effect on outflow for different cases of an active sector on the nucleus with various dust grain-size distributions. While the magnitude of the interaction is highly dependent on unknown elements of the dust grain-size, their models did show significant mass loading retardation of the flow in the dusty areas. This could explain certain aspects of the spatial structure seen in OH, particularly the fact that the sunward quadrant was consistently less extended than the others. However, the magnitude of the effect in the Combi et al. model is significantly less than is observed between the leading and trailing hemispheres in OH. Moreover, this process fails to predict a focused acceleration in the dust free zone, but rather a focused deceleration in the sunward direction.

### **7.4 Ion-Neutral Coupling:**

Photo-ionization and solar wind mass loading provide a considerable source of energy input to the trailing hemisphere of the coma that could be tapped to produce a vectored acceleration in the neutral component in a manner similar to that observed in planetary ionospheres. Newly formed ions in the inner coma are picked up by the magnetized solar wind and accelerated toward the solar wind flow direction, away from the component of the comet orbital velocity that is perpendicular to the comet-Sun line. The magnitude of the solar wind-derived acceleration will depend on the density, velocity, and field strength in the local wind,

while the orbital component will increase as the comet approaches the Sun, reaching a maximum at perihelion when the motion of the comet is greatest and directed exactly perpendicular to the comet-Sun line. The accelerating ions will mass load the solar wind, but may also in turn be mass loaded by interactions with inner coma neutrals. The strength of such an ion-neutral coupling would depend on several factors including the density of the neutral coma, which is driven by  $Q_{\text{H}_2\text{O}}$ , the ion velocity, and the different charged particle scattering cross sections of the molecular species. Detailed modeling of the ion-neutral interaction will be needed to sort out the effect, if any, of this mechanism on neutral outflow.

The possibility of an ion-neutral interaction is supported by the large gas production rate of Hale-Bopp and by observations of the inner coma ion distribution that suggest the presence of substantial mass loading of comet ions (Anderson 1997). These data show smooth acceleration of  $\text{H}_2\text{O}^+$  at  $0.161 \text{ m s}^{-2}$  on March 16, 1997 and  $0.197 \text{ m s}^{-2}$  on April 21, 1997 out to  $> 2 \times 10^6 \text{ km}$  from the nucleus. This acceleration is 3-10x smaller than was derived for Halley in 1986 (Scherb et al., 1990). Anderson (1997) attributes this retardation to solar wind mass loading by the substantial population of comet ions. Without direct measurements of the solar wind itself, it is not possible to distinguish between coupling to the solar wind and interaction with coma neutrals; both will produce the same effect.

## 8.0 Summary:

We have derived  $Q_{\text{H}_2\text{O}}$  from wide FOV images of OH emission from Hale-Bopp using aperture summation and  $V_{\text{OH}}(r)$  from fixed and variable velocity spherical expansion models that assume an unresolved  $\text{H}_2\text{O}$  source region. The resulting integrated OH brightness and  $Q_{\text{H}_2\text{O}}$  are consistent with other observations taken near perihelion, while model fits to the radial distribution of OH show a significant enhancement in the cometocentric extent of the emission relative to weaker comets. The fixed model results show conclusively that acceleration occurred over a substantial region of the coma; however, our best results are obtained with the more physically realistic variable velocity simulation, which indicates changing acceleration with cometocentric distance characterized by a steep velocity gradient inside a collision zone and a broad region of acceleration over the rest of the coma. These results confirm the extrapolated predictions of coma structure for very active comets that are based on a combination of models (Combi & Smyth 1988b) and observations (Bockelée-Morvan, et al. 1990; Schleicher, et al. 1998). When compared to published radio measurements of  $V_{\text{OH}}$  and  $Q_{\text{H}_2\text{O}}$  (Biver, et al. 1997; Colom, et al. 1997), our models match coma averages over fields of  $10^4 \text{ km}$  and  $2 \times 10^5 \text{ km}$ .

When the coma is broken down into quadrants, a significant asymmetry in the OH radial distribution emerges in the shape of the profiles on all scales within the coma. The OH brightness distributions in the trailing hemisphere are generally shallow compared to the leading

hemisphere in the inner coma, but cross over at intermediate distances to become brighter and more spatially extended. This behavior was a common characteristic of each observation and is similar to an azimuthal asymmetry observed in O(<sup>1</sup>D) by Morgenthaler, et al. (in press). Detailed study of the spatial extension shows it to be primarily focused into a 60° range of PA between the dust tail and the anti-sunward direction. Model fits for these regions suggest that greater acceleration occurred in these regions than elsewhere in the coma. We discuss several possible sources for the enhancement including a wider trailing hemispheric collision region, icy grain outgassing in the dust tail, reduced dust mass loading in the trailing hemisphere, and a vectored ion-neutral interaction with the solar wind and comet ions. Additional modeling is required to distinguish among those processes that cannot be discounted as a contributing factor.

## References:

- Anderson, C. M. 1997, *Earth Moon and Planets*, 78, 99
- Biver, N., et al. 1997, *Earth Moon and Planets*, 78, 5
- Bockelée-Morvan, D., Crovisier, J., & Gerard, E. 1990, *Astronomy and Astrophysics*, 238, 382
- Budzien, S. A., Festou, M. C., & Feldman, P. D. 1994, *Icarus*, 107, 164
- Cochran, A. L., & Schleicher, D. G. 1993, *Icarus*, 105, 235
- Colom, P., Gerard, E., Crovisier, J., Bockelée-Morvan, D., Biver, N., & Rauer, H. 1997, *Earth Moon and Planets*, 78, 37
- Combi, M. R., Kabin, K., DeZeeuw, D. L., Gombosi, T. I., & Powell, K. G. 1997, *Earth Moon and Planets*, 79, 275
- Combi, M. R., Reinard, A. A., Bertaux, J.-L., Quemerais, E., & Mäkinen, T. 2000, *Icarus*, 144, 191
- Combi, M. R., & Smyth, W. H. 1988a, *Astrophysical Journal*, 327, 1044
- . 1988b, *Astrophysical Journal*, 327, 1026
- Crifo, J. F. 1995, *Astrophysical Journal*, 445, 470
- Dello Russo, N., Mumma, M. J., DiSanti, M. A., Magee-Sauer, K., Novak, R., & Rettig, T. W. 2000, *Icarus*, 143, 324
- Farnham, T. L., Schleicher, D. G., & A'Hearn, M. F. 2000, *Icarus*, 147, 180
- Festou, M. C. 1981a, *Astronomy and Astrophysics*, 95, 69
- Haser, L. 1957, *Bulletin de la Societe Royale des Sciences de Liege*, 43, 740
- Hodges, R. R. 1990, *Icarus*, 83, 410
- Hu, H.-Y. 1990, Ph.D. Dissertation, University of Arizona
- Huebner, W. F., Keady, J. J., & Lyon, S. P. 1992, *Astrophysics and Space Science*, 195, 7
- Krishna Swamy, K. S. 1997, *Physics of comets*
- Lammerzahl, P., et al. 1987, *Astronomy and Astrophysics*, 187, 169
- Morgenthaler, J. P., et al. in press, in *Astrophysical Journal*
- Rauer, H., et al. 1997, *Science*, 275, 1909
- Samarasinha, N. H., Mueller, B. E. A., & Belton, M. J. S. 1997, *Earth Moon and Planets*, 77, 189
- Schleicher, D. G., & A'Hearn, M. F. 1988, *Astrophysical Journal*, 331, 1058
- Schleicher, D. G., Millis, R. L., & Birch, P. V. 1998, *Icarus*, 132, 397
- Schloerb, F. P. 1988, *Astrophysical Journal*, 332, 524
- Schloerb, F. P., Devries, C. H., Lovell, A. J., Irvine, W. M., Senay, M., & Wootten, H. A. 1997, *Earth Moon and Planets*, 78, 45
- Schultz, D., Li, G. S. H., Scherb, F., & Roesler, F. L. 1993, *Icarus*, 101, 95
- Smyth, W. H., Marconi, M. L., Scherb, F., & Roesler, F. L. 1993, *Astrophysical Journal*, 413, 756
- Van Dishoeck, E. F., & Dalgarno, A. 1984, in *Icarus*, 305
- Weaver, H. A., et al. 1997, *Science*, 275, 1900
- Whipple, F. L., & Huebner, W. F. 1976, *Annual Review of Astronomy and Astrophysics*, 14, 143
- Woods, T. N., Feldman, P. D., & Rottman, G. J. 2000, *Icarus*, 144, 182

## Figure Captions

**Figure 1.** The spherically averaged radial surface brightness distribution of OH on 08 April, 1997 is compared with the best fit of a model for a uniform  $0.89 \text{ km-s}^{-1}$  outflow derived from the velocity-heliocentric distance relationship of Budzien et al., 1994. The model fits the profile out to a radial distance of  $2 \times 10^5 \text{ km}$ , but begins to fall below the data beyond this point, due to collisional acceleration in the inner coma. Production rate estimates based on this fit yield  $Q_{\text{H}_2\text{O}} = 6 \times 10^{30} \text{ s}^{-1}$ , which is  $\sim 30\%$  less than those obtained from other methods (e.g. Combi et al., 2000, Colom et al., 1997).

**Figure 2.** Quadrant profiles are compared for each of the two nights. In A) and B) the four  $90^\circ$  sectors covering the anti-sun, sunward, anti-tail, and tailward directions are compared directly. While significant differences in the degree of symmetry in the coma is obvious between the nights, there is a general trend of the anti-sun and anti-tail profiles being shallow compared with the others inside of  $10^5 \text{ km}$  and then crossing over to become more extended beyond this point. In C) and D), the most radially extended quadrants of the coma are broken down into  $30^\circ$  sub-sectors of position angle and then compared with the anti-tailward sector. Each sub-sector is considerably more radially extended than the sunward profile, and are also responsible for most of the enhancement in the spherically averaged profile.

**Figure 3.** Sample model fits are shown for the spherically averaged OH radial distribution on 08 April, 1997 using the fixed velocity (a) and variable velocity (b) models. The parameters of the model outputs are shown in each case. Both models indicate the presence of acceleration over much of the coma, with the variable case providing a much closer match to  $Q_{\text{H}_2\text{O}}$  and  $V_{\text{OH}}(r)$  values obtained from other measurements.

**Figure 4.** The statistics of fit index vs. two tests of convergence for all cases in the fixed velocity model. In a), the product of the OH and  $\text{H}_2\text{O}$  velocities are shown. The convergence onto a narrow range in the cases of close fits is consistent with the two velocities tracking each other inversely in the model. In b) the ratio of the velocities reveals the degree of acceleration in the inner coma. The minimum of the distribution changes between the quadrants with the largest values occurring for the radially extended sectors. Also evident here is the overall low quality of uniform, or close to uniform, single velocity outflow, which is a value of 1 here. The fit indices for this case are  $\sim 2$  orders of magnitude larger.

**Figure 5.** The radial profile of the most extended sub-sector of the OH coma is compared here with the scaled residual dust continuum in the same sector. As can be seen here the contribution of the dust to the radial shape observed in the OH is not large enough to significantly affect the basic characteristic of the extension relative to the other sectors.

**Tables:**

Table 1. OH Observations of Hale-Bopp at the Burrell Schmidt.

Obs. Date/Time	$r^1$	$\Delta^2$	$PA_R^3$	$PA_V^4$	FOV (km)	Airmass	$Q_{H_2O}(10^{30} s^{-1})^5$
03/28/97 02:31:58	0.917	1.327	15.6	285	$4.646 \times 10^6$	2.98-3.22	$9.31 \pm 1.4$
04/08/97 02:52:14	0.920	1.418	39.8	308	$4.965 \times 10^6$	2.55-2.74	$10.8 \pm 1.6$

<sup>1</sup> Heliocentric distance in AU.

<sup>2</sup> Geocentric distance in AU.

<sup>3</sup> Position Angle of the Sun-Comet extended radius vector.

<sup>4</sup> Position Angle of the Comet Velocity Vector.

<sup>5</sup> Production rate derived from aperture summation.

Table 2. The Orbit and Solar Cycle specific photochemical parameters of OH production and fluorescence at 1 AU.

Physical Parameters of H <sub>2</sub> O Photochemistry and OH Fluorescence	
H <sub>2</sub> O Dissociation Branching Ratio	86% <sup>(1)</sup>
Dissociation Rate of H <sub>2</sub> O	$1.043 \times 10^{-5} s^{-1}$ <sup>(2)</sup>
Dissociation Rate of OH	$7.491 \times 10^{-6} s^{-1}$ <sup>(2)</sup>
OH Fluorescence g-factor	$4.54 \times 10^{-5} s^{-1}$ <sup>(3)</sup>

<sup>(1)</sup> Huebner, Keady, and Lyon, 1992

<sup>(2)</sup> Schleicher and A'Hearn, 1988

<sup>(3)</sup> Budzien et al., 1994

Table 3. At top the results of the fixed velocity simulation fits are shown as a coma average and by quadrant for both nights.

Fixed Velocity Model:						
Obs. Date	PA	$V_{\text{H}_2\text{O}}$	$V_{\text{OH}}$	$Q^{\text{H}_2\text{O}} (\times 10^{31} \text{ s}^{-1})$	Sector	
03/28/97	0-360°	0.52 ( $\pm 0.07$ )	3.25 ( $\pm 0.30$ )	1.44 ( $\pm 0.09$ )	Average	
	210-	0.56 ( $\pm 0.12$ )	2.35 ( $\pm 0.35$ )	1.30 ( $\pm 0.10$ )	Anti-Tail	
	120-	0.60 ( $\pm 0.16$ )	2.35 ( $\pm 0.35$ )	1.40 ( $\pm 0.09$ )	Sunward	
	30-120°	0.60 ( $\pm 0.08$ )	4.65 ( $\pm 0.55$ )	1.72 ( $\pm 0.11$ )	Tailward	
	300-30°	0.48 ( $\pm 0.04$ )	3.80 ( $\pm 0.50$ )	1.31 ( $\pm 0.12$ )	Anti-Sun	
04/08/97	0-360°	0.53 ( $\pm 0.07$ )	3.20 ( $\pm 0.30$ )	1.30 ( $\pm 0.05$ )	Coma Average	
	270-0°	0.56 ( $\pm 0.04$ )	2.65 ( $\pm 0.25$ )	1.19 ( $\pm 0.05$ )	Anti-Tail	
	180-	0.44 ( $\pm 0.16$ )	2.60 ( $\pm 0.50$ )	1.09 ( $\pm 0.10$ )	Sunward	
	90-180°	0.52 ( $\pm 0.08$ )	2.95 ( $\pm 0.35$ )	1.28 ( $\pm 0.06$ )	Tailward	
	0-90°	0.68 ( $\pm 0.08$ )	4.00 ( $\pm 0.30$ )	1.51 ( $\pm 0.06$ )	Anti-Sun	
Variable Velocity Model:						
03/28/97						
Sector	$V_{\text{O}}$	$V_{\text{C}}$	$V_{\text{E}}$	$dV_{\text{C}} (10^5 \text{ s}^{-1})$	$dV_{\text{F}} (10^5 \text{ s}^{-1})$	$Q_{\text{H}_2\text{O}}$
0-360°	0.94 $\pm$ 0.26	1.07 $\pm$ 0.07	2.64 $\pm$ 0.02	1.25 $\pm$ 1.25	0.20 $\pm$ 0.01	9.70 $\pm$ 0.55
30-120°	0.88 $\pm$ 0.10	0.88 $\pm$ 0.10	1.78 $\pm$ 0.25	0.0	0.15 $\pm$ 0.06	8.95 $\pm$ 1.10
120-210°	0.94 $\pm$ 0.10	0.94 $\pm$ 0.10	1.74 $\pm$ 0.25	0.0	0.14 $\pm$ 0.05	9.80 $\pm$ 0.77
210-300°	1.05 $\pm$ 0.30	1.36 $\pm$ 0.15	2.10 $\pm$ 0.20	3.1 $\pm$ 2.0	0.11 $\pm$ 0.04	11.5 $\pm$ 1.1
300-30°	1.02 $\pm$ 0.33	1.21 $\pm$ 0.13	2.22 $\pm$ 0.32	1.9 $\pm$ 1.5	0.14 $\pm$ 0.07	8.85 $\pm$ 0.55
04/08/97						
0-360°	0.94 $\pm$ 0.10	1.14 $\pm$ 0.22	2.52 $\pm$ 0.25	2.0 $\pm$ 1.8	0.24 $\pm$ 0.07	9.30 $\pm$ 0.60
0-90°	0.90 $\pm$ 0.10	1.04 $\pm$ 0.10	2.24 $\pm$ 0.50	1.4 $\pm$ 1.3	0.21 $\pm$ 0.10	9.13 $\pm$ 0.31
90-180°	0.88 $\pm$ 0.17	0.94 $\pm$ 0.12	2.50 $\pm$ 0.50	0.6 $\pm$ 0.5	0.27 $\pm$ 0.08	8.70 $\pm$ 0.59
180-270°	1.02 $\pm$ 0.30	1.16 $\pm$ 0.16	2.65 $\pm$ 0.35	1.2 $\pm$ 1.0	0.23 $\pm$ 0.08	10.1 $\pm$ 0.9
270-360°	1.05 $\pm$ 0.35	1.43 $\pm$ 0.20	2.70 $\pm$ 0.24	3.8 $\pm$ 3.0	0.19 $\pm$ 0.05	11.1 $\pm$ 1.0

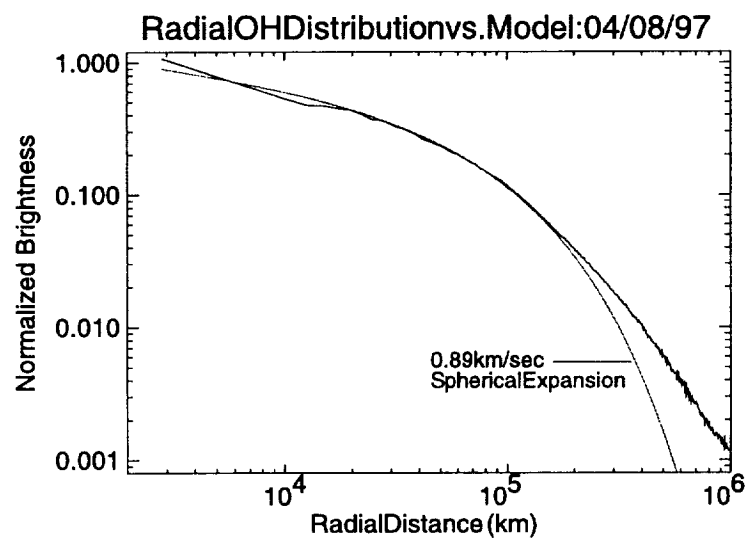


Figure 1

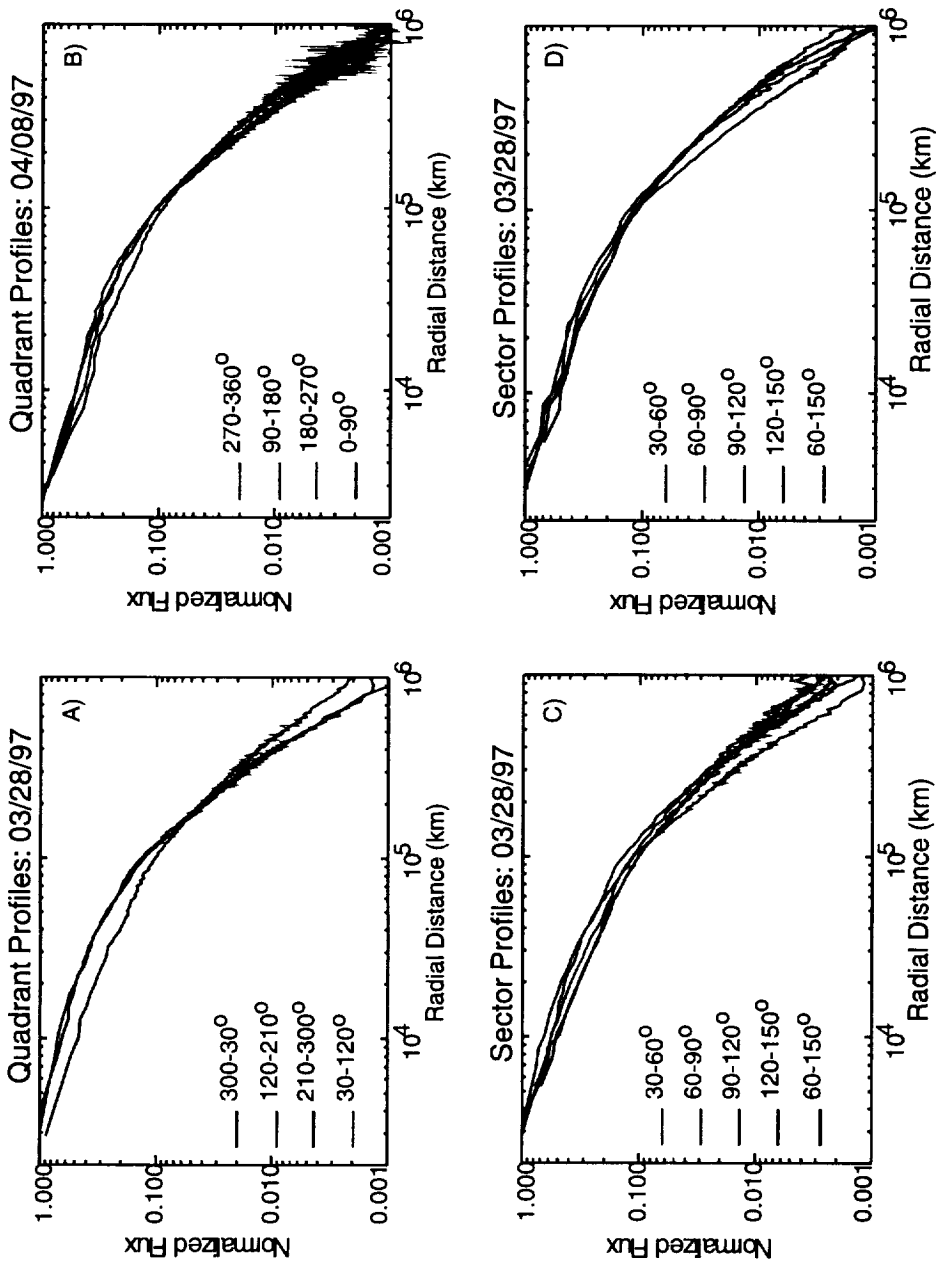


Figure 2

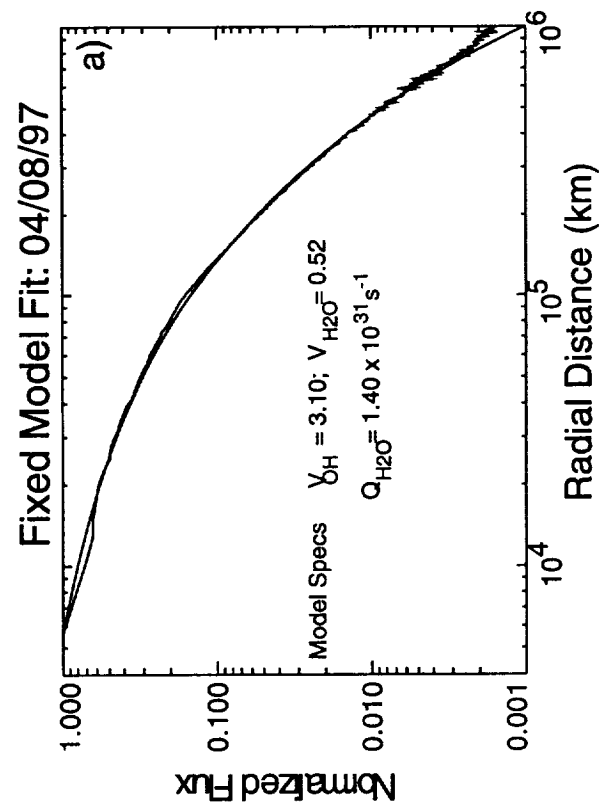
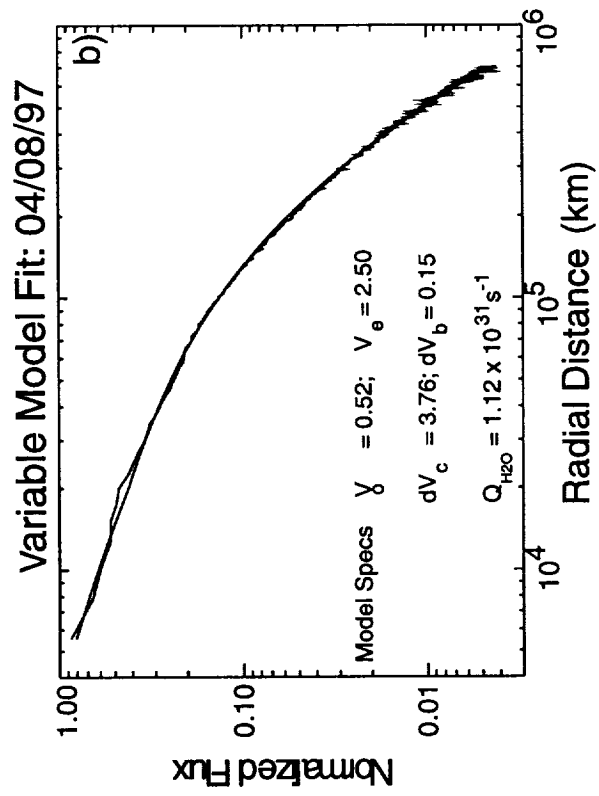


Figure 3

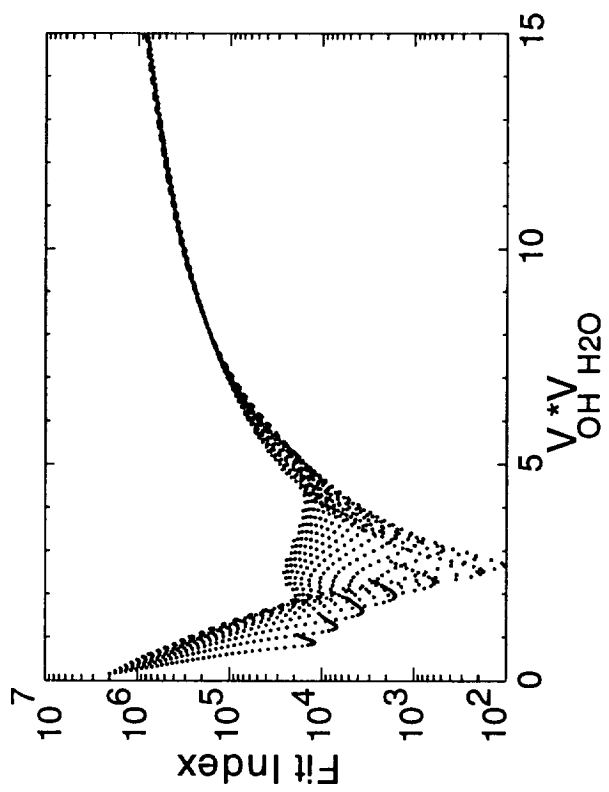
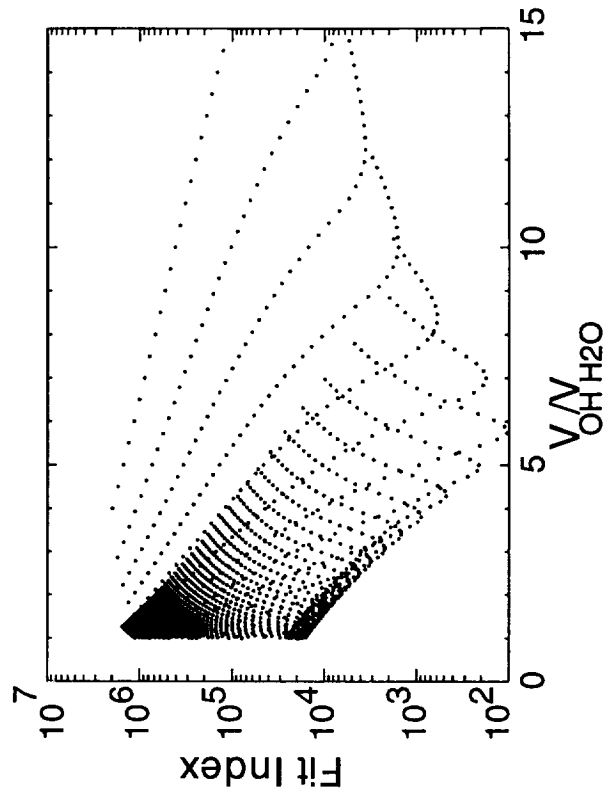


Figure 4

# OHRadialProfile vs.ContinuumContribution

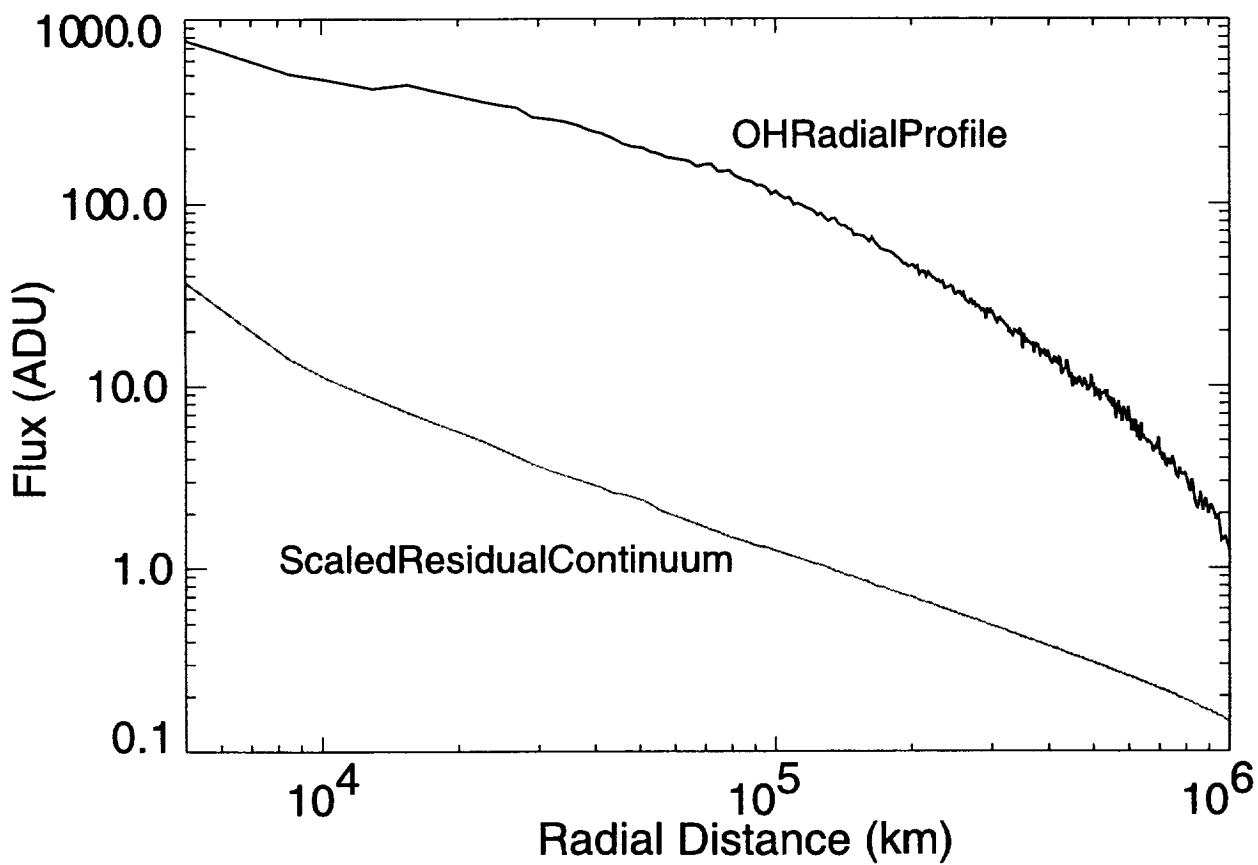


Figure 5